JOURNAL OF GEOPHYSICAL RESEARCH, VOL. 106, NO. A4, PAGES 5987–6006, APRIL 1, 2001

Wave power studies of cusp crossings with the Polar satellite

V. Angelopoulos, F. S. Mozer, J. Bonnell, M. Temerin, and M. Somoza

Space Sciences Laboratory, University of California, Berkeley

W. K. Peterson and H. L. Collin

Lockheed Martin Space Physics Laboratory, Palo Alto, California

B. Giles

NASA Goddard Space Flight Center, Greenbelt, Maryland

Abstract. Burst data from the electric field instrument (EFI) on the Polar satellite are used to classify cusp wave properties and the association of the observed waves with particle populations. The most intense wave type (most commonly triggering burst mode data collection) are the broadbanded waves which are then studied in detail using the three-dimensional resolution of the EFI. Finite wavelength effects are removed using two techniques: time-shifting of the sphere potentials to a spacecraft body reference time and spin angle selection. The corrected electric field signal exhibits a uniform spectrum in two dimensions. The wave properties are consistent with two-dimensional turbulence, with phase velocities smaller than the spacecraft velocity and frequency as low as (or lower than) the oxygen gyrofrequency. Owing to their low frequency, we conclude that these waves cannot resonate with and thus heat the ions. The broad k-spectrum and very low frequency in the plasma frame points toward drift or shear instabilities for wave excitation.

1. Introduction

Ion conic formation at the Polar cusp is an important mechanism for populating the magnetospheric plasma [*Yau and André*, 1997]. The heating mechanism of cusp ions leading to their eventual escape up the field lines due to the mirror force is still an area of active research. Transversely accelerated ions in the auroral ionosphere are seen in regions of general wave activity and correlate with broadband low-frequency waves in particular [*André and Yau*, 1997]. This correlation has also been noted for the cusp [*André et al.*, 1988] and its vicinity [*Kintner et al.*, 1996], though the correlation is not one-to-one, as other types of waves may coexist or replace the occurrence of broadband low-frequency waves [e.g., *Peterson et al.*, 1986]. The variations in the wave characteristics may be due to the presence of density depletions and gradients [*Kintner et al.*, 1996] or the presence of a cool, low-density electron population [*André et al.*, 1987].

Broadband low-frequency waves have been known to exist in the auroral zone from DE 1 [*Gurnett et al.*, 1984], Viking [*André et al.*, 1987], Freja [*André et al.*, 1998], and rockets [*Kintner et al.*, 1996] at altitudes from a few hundred to >20,000 km [*Huddleston et al.*, 2000]. The nature of the waves is primarily electrostatic, with a magnetic component that decreases with altitude or frequency faster than the electric field component. The nature of these waves is not understood. At issue is whether the observed wave power is due to temporal fluctuations (such as Alfvén waves propagating down the field line) or spatial irregularities with low (or zero) frequency at the plasma frame but Doppler-shifted to the observed frequencies owing to the relative motion of plasma and the observing platform [*Gurnett et al.*, 1984]. The possibility that some portion of the observed wave power may be temporal and that the good correlation between waves with transversely accelerated ions, led to the hypothesis that ion cyclotron resonant heating with the left-hand-Polarized component of the waves may heat the ions to their observed perpendicular temperatures [*Chang et al.*, 1986]. This general model was applied to the cusp ion conics with relative success since only 10% of the observed wave power there is needed to explain the observed ion heating [*André et al.*, 1988, 1990].

However, the realization that broadbanded waves may be due to Doppler shift of spatial structures [*Temerin*, 1978, 1979] and that at least occasionally the broadband nature of the power spectrum may be due to spiky (soli-

Paper number 2000JA900127.
0148-0227/01/2000JA900127$09.00

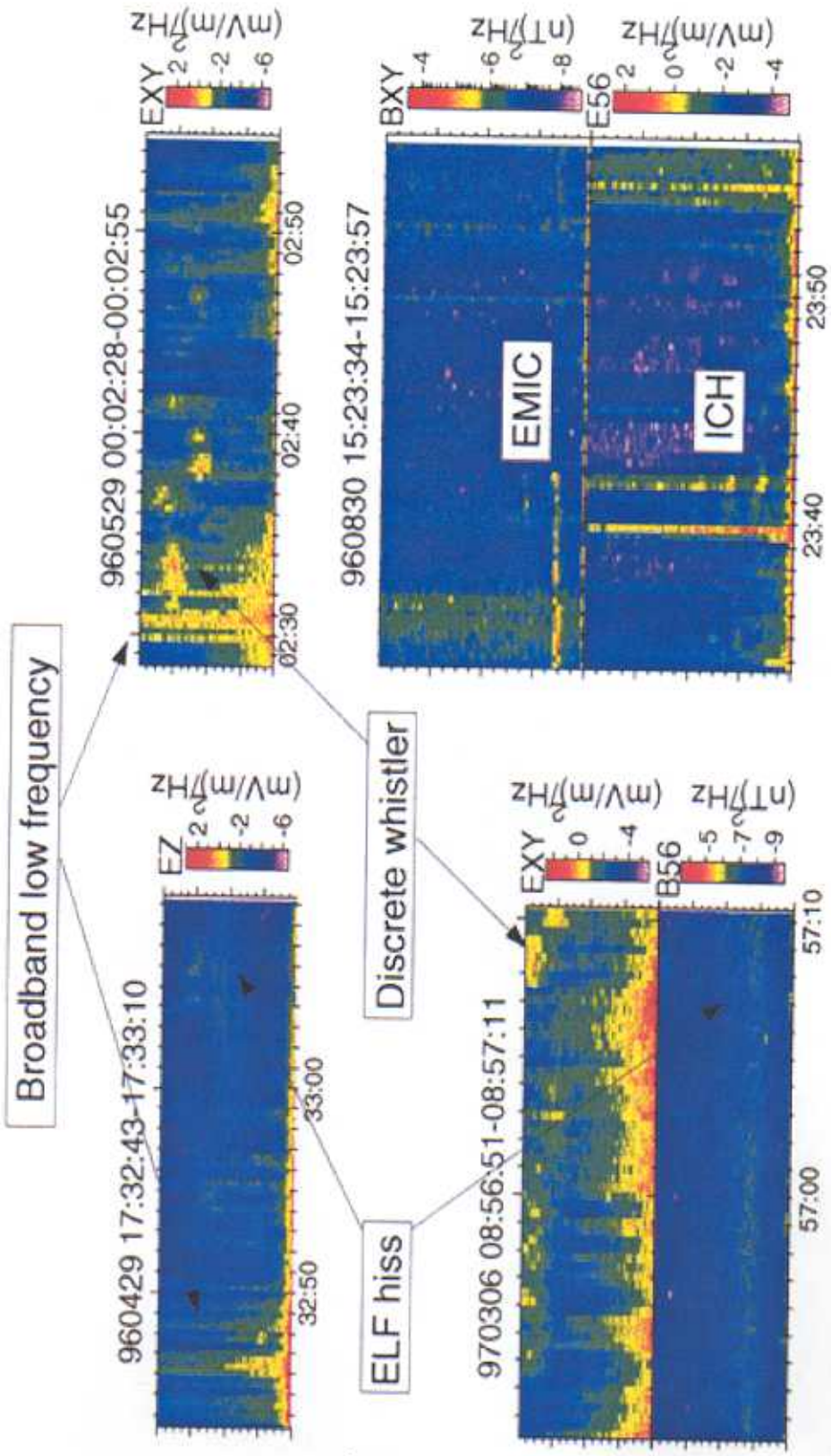

Plate 1. Types of waves observed in the cusp by the electric field instrument (EFI)/Polar instrument.

tary) electric field structures [*Huddleston et al.*, 2000] calls for a re-examination of the supposition of the temporal nature of the waves. The availability of high-resolution (burst mode) time series of three-dimensional electric and magnetic data from the Polar satellite permits a thorough reexamination of this issue. We focus on the Earth's cusp in recognition of its importance for ion acceleration.

We first study the types of waves observed in the cusp using the electric field instrument (EFI) on board the Polar satellite. EFI burst mode data are collected typically for ~5-hour periods per orbit, and the largest-amplitude signals observed during a 25 s (for 1600 vectors s^{-1} storage rate) or 5 sec (for 8000 vectors s^{-1} storage rate) interval within each of these time periods are transmitted to the ground. The period of burst collection is commandable from the ground, while the number of bursts collected per orbit varies according to onboard memory resources. During the first year of EFI operations it was decided that one burst collection per orbit would be allocated to dayside perigee auroral crossings. These are the data we focus on in this paper.

We first search for the most common wave type (i.e., the one which most commonly exhibits the highest amplitude), and we identify it to be the broadband low-frequency wave type. We then show that ion beams/conics are simultaneously (within the 25 s of the burst duration) observed on the Toroidal Imaging Mass-Angle Spectrograph (TIMAS) and Thermal Ion Dynamics Experiment (TIDE) instruments in confirmation of earlier correlative studies performed throughout the auroral oval. We subsequently study this dominant wave type in detail. In section 3 we examine the origin of its spectral power and show that the enhanced power is most often due to E field irregularities and not always due to spiky fields. The amplitude of the irregularities is affected significantly by spatial (i.e., very low frequency) structures convected past the satellite owing to its motion. We correct for that effect by performing a spin-phase-dependent time lag of the probe voltage time series. Finite wavelength effects are also minimized by a spin-phase selection for antenna directions mostly perpendicular to the spacecraft velocity. The resultant agreement between the spin axis and ram direction spectra shows that the wave power is due to isotropic two-dimensional (2-D) turbulence. In section 4 we interpret the spread in the cross correlation as due to the phase-velocity effect. This permits us to determine, in section 5, the dominant phase velocity and frequency as a function of wave number. The resultant frequency (which is below the oxygen gyrofrequency for wavelengths at or above the ion gyroradius) and the broad k-spectrum suggest that the 2-D turbulence is excited by a broad k-spectrum instability mechanism such as drift waves, shear flows, or dispersive Alfvén waves.

2. Statistical Studies of Particles and Waves

2.1. Data Sets and Coordinate systems

We examined burst data collected by the EFI [*Harvey et al.*, 1995] on the Polar satellite's perigee crossings of the Polar cusp during the period March 1, 1996, to May 31, 1997. Polar has a low (5700 km) perigee, a high (~9 R_E) apogee, and an orbital period of 18 hours, and it spins in a cartwheel mode with a 6-s spin period. The EFI is composed of four spin plane wire booms (two of them are ~55-m-long wire booms, and the other two are 65 m long) and two spin axis stacer booms (6.7 m long). A single sphere, numbered 1 through 6, is mounted at the end of each boom and is current-biased to measure the plasma potential referenced to the spacecraft potential. Spin plane pairs 12 and 34 and spin axis pair 56 form an orthogonal triad which measures the three components of the electric field at 40 samples s^{-1}, and collects a "burst" of data at 1600 or 8000 samples s^{-1} twice per perigee pass. In a noon-midnight orbit, burst selection occurs typically once at the dayside (cusp) and once at the nightside and is selected as the sector of waveform data with the highest amplitude electric field. Most often, the perigee pass dayside bursts take place within the cusp proper.

The natural coordinate system for electric field quantities is the (XY, Z, 56) system. This is a de-spun coordinate system that preserves the separation between spin axis and spin plane components of the field. This separation is useful because the spin axis and the spin plane component offsets respond quite differently to ambient plasma conditions. XY points along the intersection between the spin plane and the ecliptic plane (this season XY was positive away from the Sun); Z points perpendicular to XY in the spin plane, positive northward; and 56 is along the spin axis and forms a right-hand system with the other two axes (in this season, 56 was positive duskward). When interested in the non-DC part of the field, the offsets have little importance, and it is possible to view the data in another, more natural coordinate system. This is the (Epar, Eperon, Eperoff) system. Epar is the component of the electric field along the instantaneous magnetic field direction. Eperon is the component normal to the magnetic field but on the spin plane (i.e., it lies on the intersection of the magnetic field-normal plane and the spin plane, positive toward north) while Eperoff completes the orthogonal, right-hand system. A benefit of using this system when the field is near the field plane is that it keeps the contributions from the shorter, 56 booms mainly on one component (Eperoff), and it preserves the independence of the other field-normal component (Eperoff) from the 56-boom measurement.

Ancillary data used in this study are from the following: the Toroidal Imaging Mass-Angle Spectrograph

(TIMAS) instrument [*Shelley et al.*, 1995], which measures twice per spin the major ion species with 4π sr angular coverage in the energy range 15 eV-32 keV. For the purposes of this work we used TIMAS distribution functions and spectrograms at 22.5° angular resolution and 6-s temporal resolution; the thermal ion dynamics experiment (TIDE) instrument [*Moore et al.*, 1995], which measures the masses of the dominant ions in the range 0.1-500 eV at 6-s resolution in full three dimensions. To study all our events we used distribution function plots at 6-s resolution with an angular resolution of $11.25° \times 22.5° \times 7°$; the plasma wave instrument (PWI) [*Gurnett et al.*, 1995], which employs three search coils to measure the three orthogonal AC components of the magnetic field. Its waveforms during EFI burst collection are captured by the EFI's data processing unit and are transmitted at the same time resolution as the EFI bursts. For the purposes of this paper we used the time series burst signals, which we processed just as the EFI signals; the Magnetic Field Experiment (MFE) instrument [*Russell et al.*, 1995], which measures the ambient magnetic field from DC up to 100 Hz. For the purposes of this work we used data at 0.12-s resolution.

2.2. Wave and Particle Statistics

For the purpose of a statistical examination of the dominant wave mode within the cusp, we identified 53 EFI perigee bursts of putative cusp crossings occurring at magnetic local times within ±2 hours of noon. We checked using the TIMAS data to ensure that the particle signatures are commensurate with those of the cusp or the adjacent boundary layer by ensuring the presence of magnetosheath particles when that was possible. For the 39 events when TIMAS was neither off nor in an unfavorable mode of operation, only two events were excluded as noncusp/nonboundary layer events. TIDE was off during those two events.

We examined the spectral characteristics of the observed waves in E and B fields. Plate 1 shows typical wave signatures of the burst collection. These are classified into five types: (1) Broadband low-frequency waves, exhibiting high-power spectral densities from DC up to several times the proton gyrofrequency, and often extending beyond the maximum frequency resolved by the EFI sampling rate. These waves have been studied before in the cusp and in the auroral zone in general as discussed in section 1. (2) ELF hiss (electromagnetic) waves, exhibiting a broad peak above the two-ion cutoff frequency (between the proton and helium gyrofrequencies) [*Gurnett and Burns*, 1968]. This is thought to be generated in the equatorial magnetosphere, within the plasmasphere and to leak to the high-latitude cusp [*Russell et al.*, 1970]. Such leakage is also evident when magnetic spectrograms from the loop antenna from the PWI instrument are examined during the times of ELF hiss observations. These spectrograms clearly show a continuous band of plasmaspheric hiss (a dominant wave mode in the plasmasphere) extending into the cusp region. (3) Discrete whistler (electrostatic) waves, with narrow spectral peaks, often appearing as series of bursts of 0.1-1 s duration. The waves (also referred to as lower hybrid waves) are usually seen just above the low hybrid frequency cutoff f_{lh}. Infrequently, a magnetic component to the signal can be visible when these waves are at several times f_{lh}. The frequency peak may change abruptly with time. Assuming a density in the range of a few to 10 particles cm^{-3} in the cusp, and a fraction of the total ion density in O^+ (0.1-0.5), we obtain f_{lh} ~150-800 Hz, i.e., a wide range of values. Abrupt changes in f_{lh} may be caused by O^+ beams and density striations, explaining the peak emission frequency jumps. The waves are thought to be generated by keV beams of precipitating particles [*André et al.*, 1986, 1994]. (4) Ion cyclotron (electrostatic) waves, which extend for multiple harmonics and appear either in bursts or in a continuous fashion (both seen on the same panel of Plate 1). The origin of the multiple harmonics may be nonlinear steepening of cyclotron waves [*Temerin et al.*, 1979] or spiky fields emitted at the cyclotron period [*Ergun et al.*, 1998a]. (5) Electromagnetic ion cyclotron waves, which are typically seen below the first and possibly second harmonic [*Gurnett and Frank*, 1972], likely generated by electron beams [*Temerin and Lysak*, 1984] and are continuous over one-to-tens of seconds.

Figure 1 presents the occurrence frequency of each wave type within the ensemble of EFI cusp crossings. Broadbanded low-frequency waves are present in all cusp crossings, with the next most frequent wave type, the ELF hiss, seen ~60% of the time. ELF hiss amplitudes are typically an order of magnitude lower than broadbanded waves. A similar argument holds for discrete whistlers: Because of their narrow spectral width, the integrated power and thus amplitude are typically small, i.e., smaller than that for broadbanded waves. The next most common wave type, electrostatic ion cyclotron waves, have amplitudes similar to the broadbanded waves and are seen typically in the same 25-s burst as the EMIC waves. Since the cyclotron waves are seen less than 50% of the time, it is evident that >50% of the cusp bursts are collected because the peak electric field amplitude is of the broadbanded wave type. Because of their broadbanded nature and extension to low frequencies (where the power spectral density is typically the largest), these waves have the largest power content in each crossing. Plate 2 shows an example of such a crossing on March 18, 1996. The EFI signatures are shown at the nominal (40 samples s^{-1}) resolution in the (XY, Z, 56) and the (Epar, Eperon, Eperoff) systems. TIMAS data accompany the fields measurements and show the presence of upflowing H^+ and O^+ around the time of increased E field fluctuations. Ion fluences peak near the times of peak E field amplitudes and thus coincide with EFI burst collection. The observed waves are Polarized perpendicular to the magnetic field

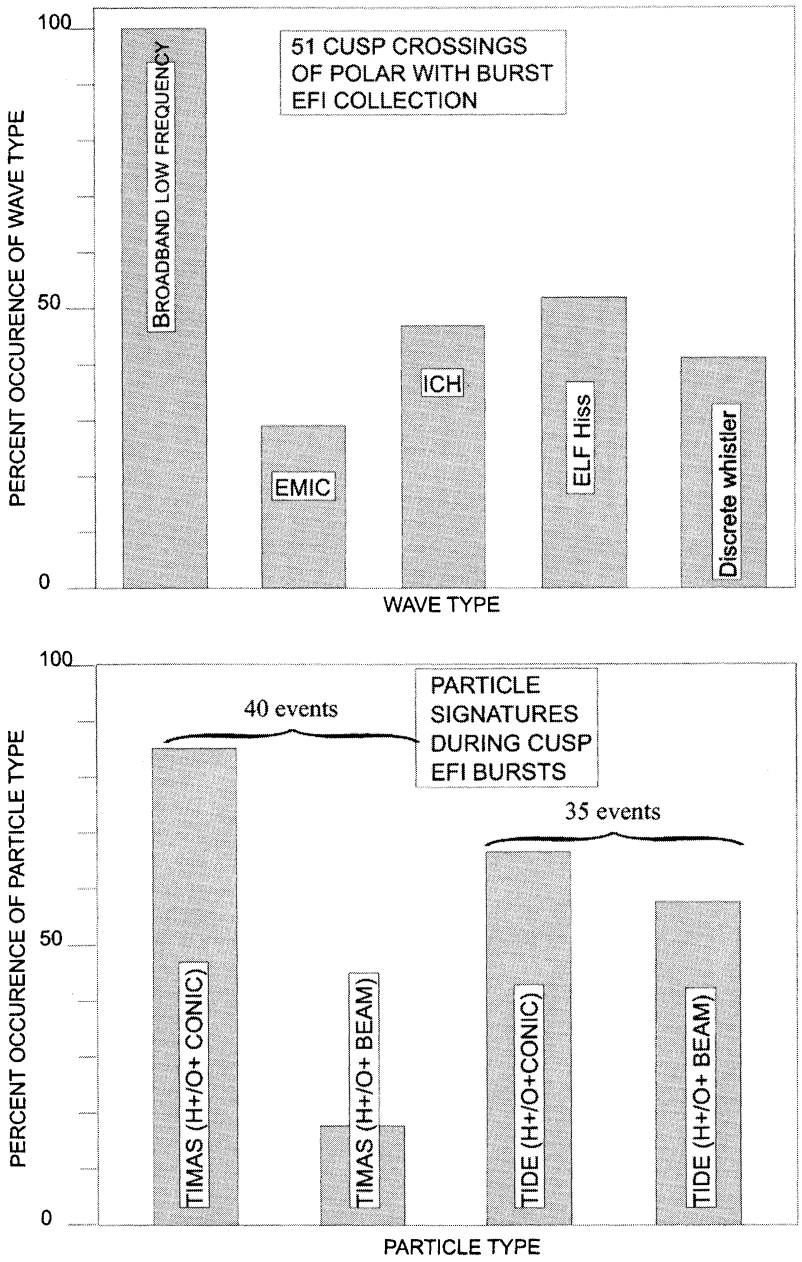

Figure 1. (top) Occurrence rates of different wave types based on the EFI instrument. (bottom) Occurrence rates of different particle types based on the Toroidal Imaging Mass-Angle Spectrograph (TIMAS) and Thermal Ion Dynamics Experiment (TIDE) instruments. Particles and fields data sets are studied during EFI burst collection within ± 2 hours of noon which coincides with cusp encounters.

as evidenced by the small value of the Epar component relative to the other two components. The remaining power in the Epar component is consistent with noise.

TIMAS H^+ and O^+ distribution functions in parallel-perpendicular velocity space for the March 18, 1996, event are shown in Plate 3. These are collected every 6 s but are shown here every 12 s. The spacecraft velocity has not been subtracted explaining, in part, the offset in the perpendicular direction which is present in Plate 3. Time aliasing may also affect the shape of the distributions, since the ion populations are quite variable. However, it is evident that the upflowing oxygen and proton populations are conics of typical perpendicular temperature ~110 and 75 eV (thermal velocities of 150 and 30 km s^{-1}, respectively).

Figure 1 also shows (at the bottom) the statistical occurrence of ion beams/conics seen in concurrence with the EFI burst events collected. Most intense EFI events (bursts) correlate with the presence of ion conics. The low time resolution in the plasma data prohibits a one-to-one association of the conics with EFI broadband wave power intensification.

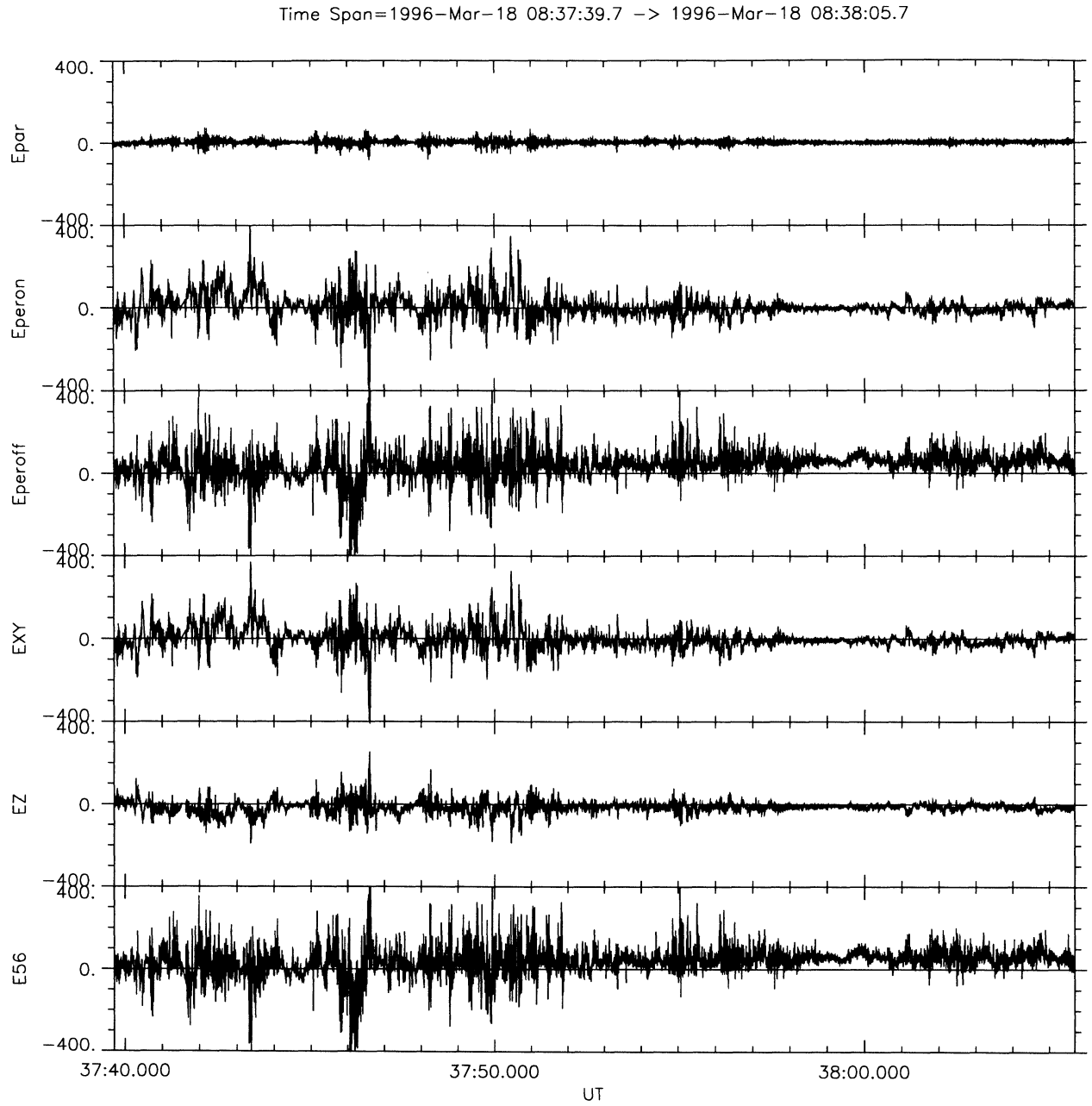

Figure 2. Time series of burst data at 1600 samples s^{-1} resolution for the event of Plate 2.

Figure 2 shows the time series of the burst data collected in the event of March 18, 1996. Irregular fluctuations, i.e., no evident coherent waves, are responsible for the broadbanded nature of the spectral power. While spiky fields are seen a few times in this event (e.g., at 0837:46.6 UT) and occasionally during others in our burst event collection, most of the spectral density enhancement is due to the irregular fluctuations.

The dynamic power spectra of the electric and magnetic field fluctuations perpendicular to the magnetic field are shown in Plate 4. The Eperoff component of the electric field and its orthogonal magnetic field (in the peron direction, termed "Scoilperon" in Plate 4) were chosen. The dynamic spectrograms are shown in the center of the plot, while representative line spectra are shown at the top and representative time series are shown at the bottom. Note that the line spectra of the magnetic field (blue lines, in $nT^2\ Hz^{-1}$) were multiplied by 10^4 in order to fit in the same panel as the line spectra of the electric field (red lines, in $mV^2\ m^{-1}$). It is evident that the electric field power spectral density is elevated and broadbanded throughout almost the entire interval. This is most of the time due to random fluctuations of the electric field as shown in the bottom left time series. Occasionally, a spiky field occurrence, interpreted as an electrostatic shock [*Mozer et al.*, 1977], will

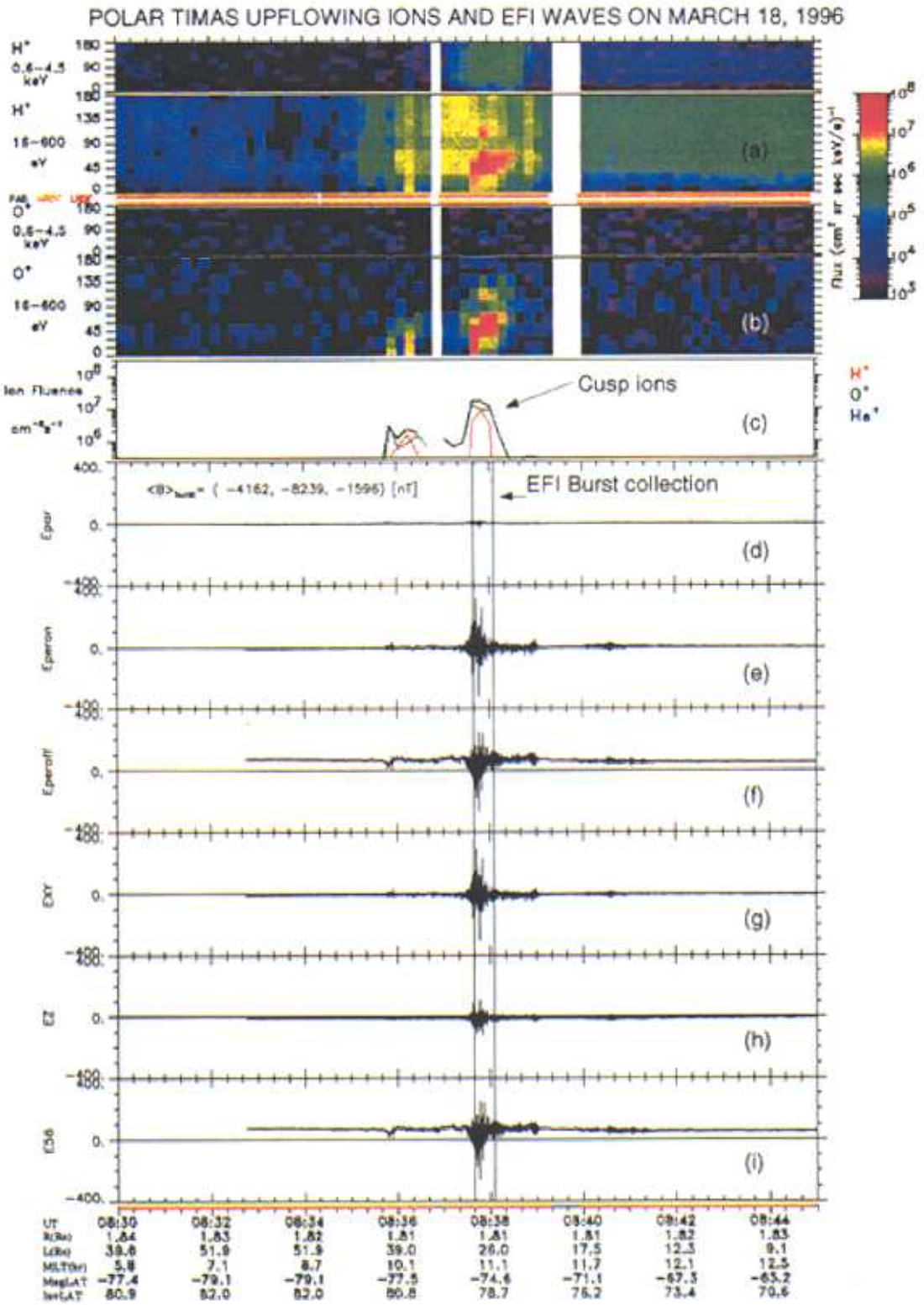

Plate 2. (a-i) Overview of a cusp crossing in EFI and TIMAS data sets. Increased electric field fluctuations (triggering burst mode onset) and upflowing ions are observed in the cusp. The EFI data at 40 samples s^{-1} are shown in the $(XY, Z, 56)$ coordinate system (Plates 2g-2i) and the (Eper, Eperon, Eperoff) coordinate system (Plates 2d-2f). Epar is consistent with zero.

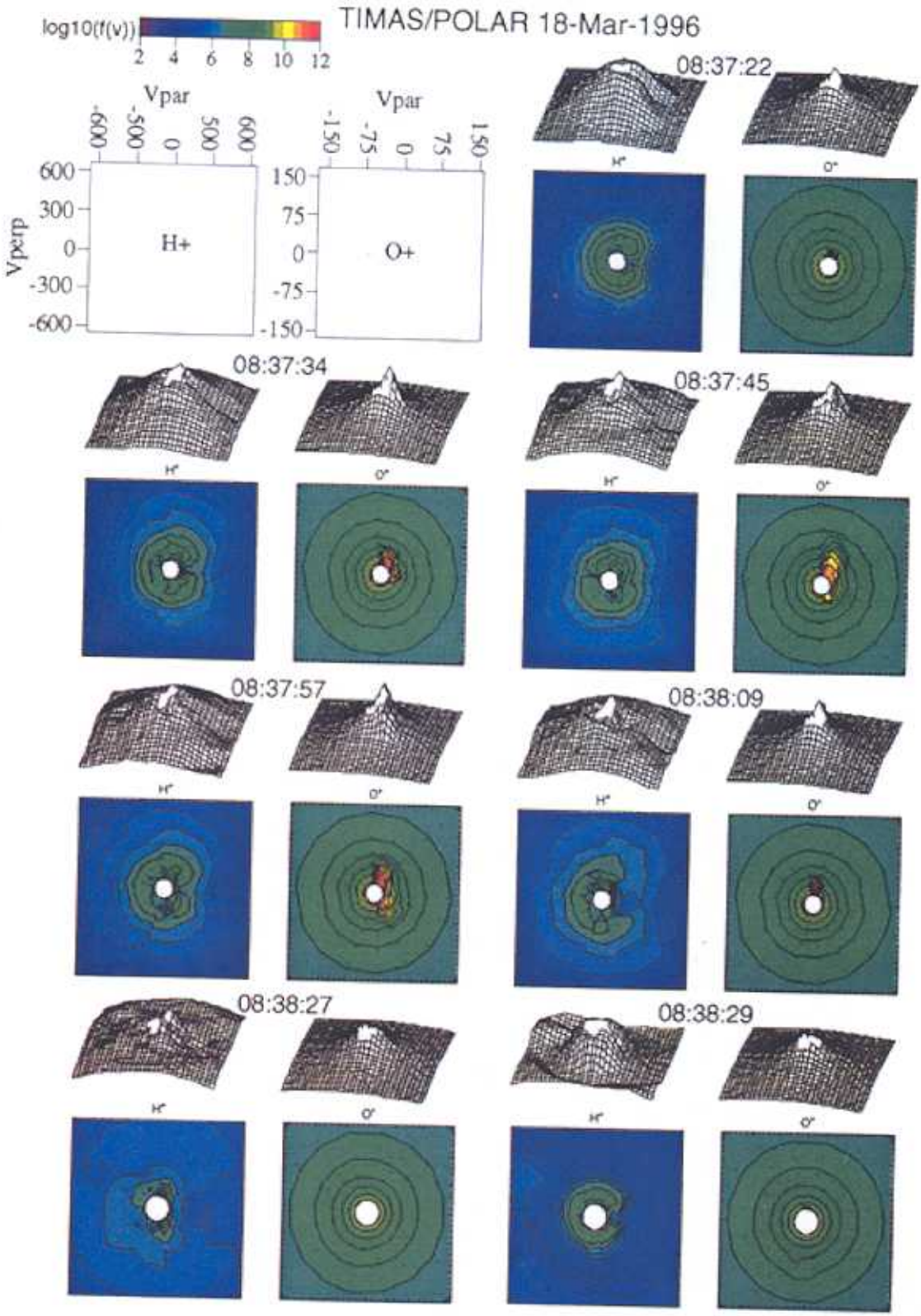

Plate 3. Detailed oxygen and hydrogen ion distributions from the TIMAS instrument for the event of Plate 2. Ion conics are evident during the EFI burst data collection. Beams or conics were observed during all EFI bursts in the cusp database assembled for this study.

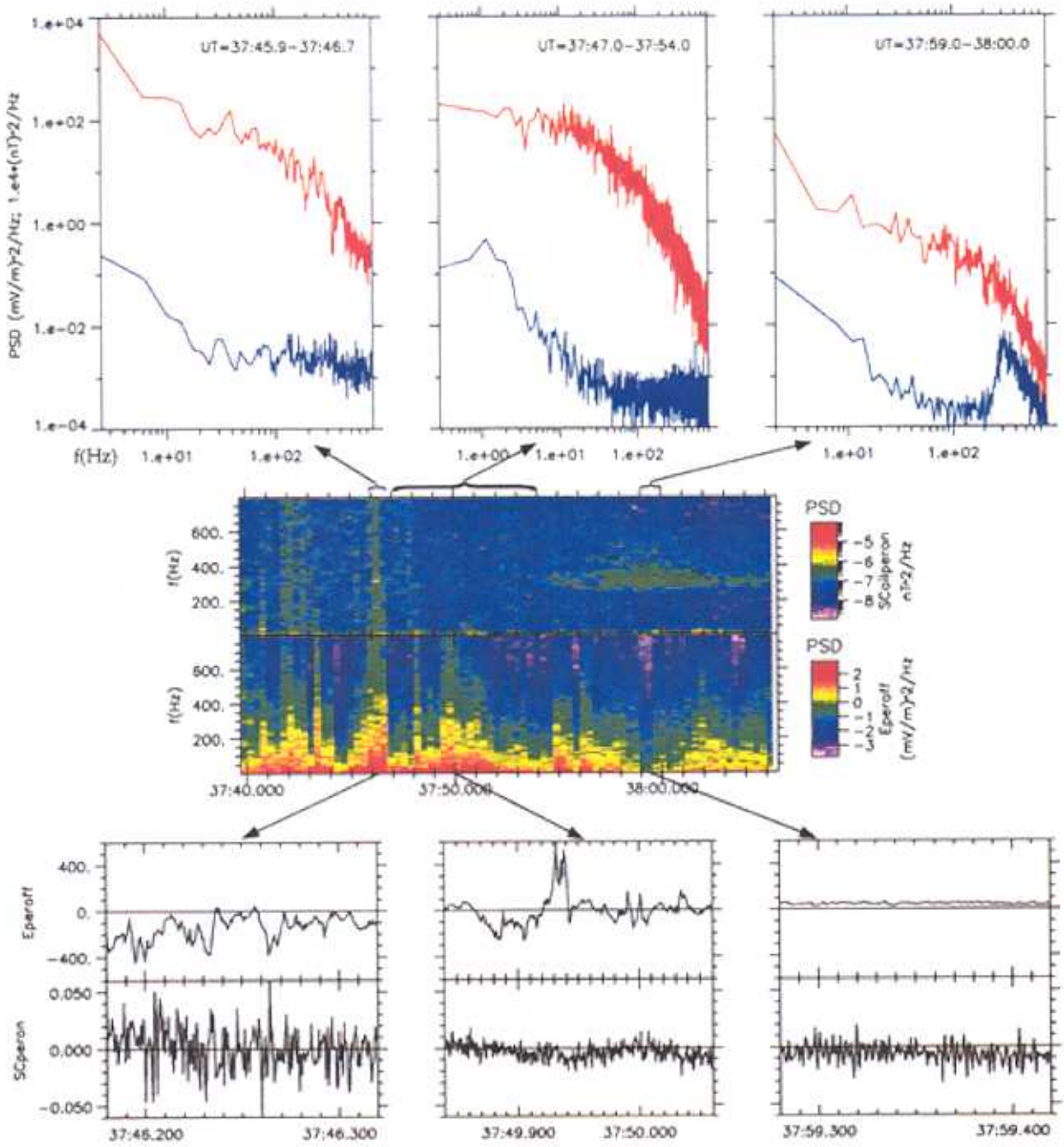

Plate 4. Magnetic and electric field dynamic power spectra (center) along with sample line spectra (top) and sample time series (bottom) at selected times noted by the arrows. Note that the magnetic field line spectra (blue) have been multiplied by 10^4 to fit in the same (top) panels as the electric field spectra (red).

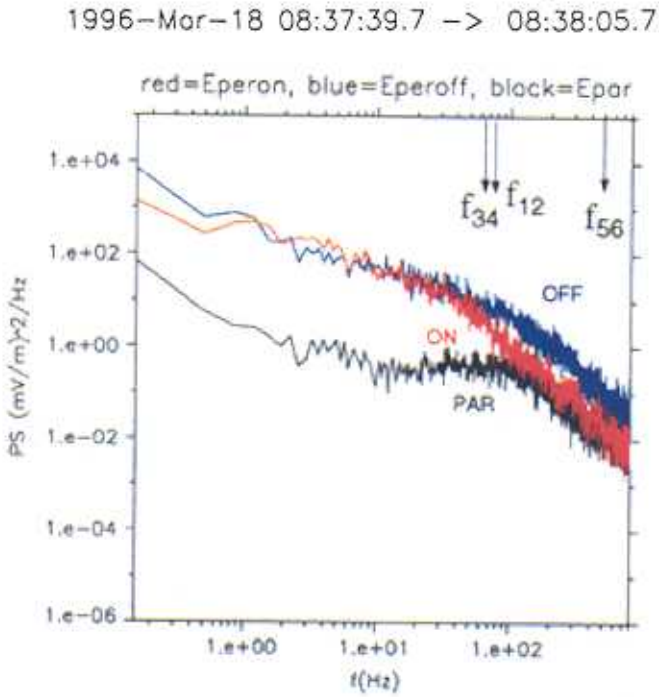

Plate 5. Power spectral density for the cusp crossing event of Plate 2. Note that f_{12} is the frequency in the spacecraft frame which corresponds to spatial structures of wavelength equal to the 12 interprobe distance, d_{12}, Doppler-shifted owing to the spacecraft velocity V_{sc}, i.e., $f_{12} = V_{sc}/d_{12}$. The same holds for the other frequencies.

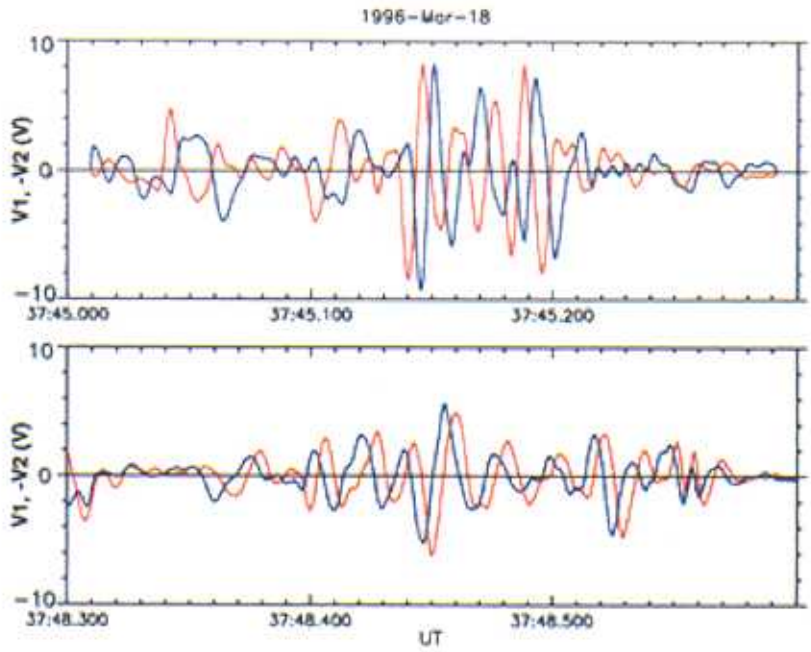

Plate 6. Time series data of the potential in sphere 1 (V1) and the negative potential in sphere 2 (-V2) during two times. (top) When sphere 1 is ahead of sphere 2 in its motion through the plasma. (bottom) Three seconds (half a spin) later, when sphere 1 is behind sphere 2 in its motion through the plasma. The time series of sphere potentials indicate a time lag that is consistent with motion of the spheres through spatial irregularities.

contribute to the broadbanded nature of the spectrum, as shown in the center time series panel at (mm:ss.msec =) 37:49.930 UT.

At the times of broadbanded waves the magnetic field signature above ~20 Hz has a flat spectrum indicative of reaching instrument sensitivity (center bottom panel time series, center top panel line spectra). There are two exceptions to that: (1) When shortlived broadbanded noise is evident in the spectrograms such as for a <0.5 duration around 37:42.250 UT (expanded in the left bottom panel time series). This corresponds to large-amplitude solitary structures [*Mozer et al.,* 1997; *Ergun et al.,* 1998b], which are undersampled at the current sampling rate of 1600 samples s^{-1} (they typically last 50-200 μs). (2) When ELF hiss is present as in the interval after 37:54.000 UT. To show that this is uncorrelated with the electric field broadband noise, we have selected to present the time series and detailed line spectra of ELF hiss when the broadband noise power has a minimum (37:59.300 UT). Evidently, a coherent magnetic signature at 3-ms period has no counterpart in electric field data. Below ~20Hz the magnetic field spectral density is a decreasing function of frequency, but appropriate calibration of the amplitude and phase is quite important for a quantitative assessment of the coherence and amplitude ratios of E and B. We note, however, that as expected from previous studies of broadband waves [*Gurnett et al.,* 1984], the magnetic field spectral power decreases with frequency faster than that of the electric field, even after restoration of the magnetic field amplitude using preliminary calibration data.

After this brief summary of the waves seen in the burst event chosen, we turn to the detailed study of the electric field data. The spectrum in the three components of the electric field (Epar, Eperon, Eperoff) is shown in Plate 5. At this time (B~9400 nT) the proton and oxygen gyrofrequencies are $f_{O+} = 9$ Hz and $f_{H+} = 140$ Hz. No spectral peak at those frequencies is evident in the power spectra.

On the basis of the concurrence of broadband waves and accelerated ions described above, it might be tempting to associate the two phenomena causally. However, there are two reasons to discount the notion that the waves cause the perpendicular ion heating. First, the conics are rarely observed at 90° pitch angles. In fact, most often they are confined within 60° of the magnetic field, indicating that they were heated well below the Polar altitude. Second, the power associated with the waves is excessive. Specifically, if we take the observed spectral densities in the frequency band of f_{O+} and f_{H+} (10^2 $(mV/m)^2$ Hz^{-1} and $2(mV/m)^2$ Hz^{-1}, respectively), the above theory [see *Chang et al.,* 1986, equation (3)] predicts heating rates of 300 and 100 eV s^{-1}, respectively, for the two species. Heating to the observed 110 and 75 eV range is expected within 0.4 s for the O^+ and 0.75 s for the H^+. The O^+ and H^+ conics exhibit a thermal spread in parallel velocity space of ~20 and 50 km s^{-1}, respectively. Thus heating should occur within an 8-km altitude for the O^+ and a 37-km altitude for the H^+. Given the model variation of the field at Polar altitudes (1.81 R_E), we obtain from first adiabatic invariant conservation that the O^+ and H^+ conics should be peaked within 4° and 8° from the field normal, respectively. Thus they should be indistinguishable from strictly perpendicular conics given the 22.5° and 11.25° angular resolution of the TIMAS and TIDE instruments utilized. However, this is not the case in the observed distribution functions which exhibit clear conic structure at pitch angles of ~60°. The apparent rate of heating is a factor of 10 or so slower than the value obtained from the average spectral density of $10^2(mV/m)^2$ Hz^{-1} and $2(mV/m)^2$ Hz^{-1} at f_{O+} and f_{H+}, respectively; the discrepancy worsens by another order of magnitude if instead of the average power spectrum shown in Plate 5, we consider the power spectrum at those times that the broadband waves are most prevalent. These observations apply not only to the specific event chosen but to all events in our database, since spectral densities and conic/beam behavior are similar in our events.

In sections 3-5 we explain why the observed large spectral density is a simple reflection of the spacecraft's motion through predominantly spatial structures rather than temporal wave power. As such, it is not applicable for explaining ion heating. Rather, we will see that the spectral shape and dominant frequency provide evidence for operation of instabilities driven unstable by density gradients or velocity shear.

3. Detailed Case Study of Dominant Wave Type

Before we embark upon a detailed study of the time series of the probe potentials and the associated electric field, we make the following observation in Figure 2 and Plate 5: While it is understandable in Figure 2 and Plate 5 why the parallel wave power is reduced (indicating the absence of a field-aligned component to the perturbation), it is not immediately clear why the spin plane component fluctuation amplitudes and power are consistently below the spin axis power at frequencies above ~40 Hz. In other words, it is not immediately obvious why the fluctuations in XY are smaller than those in 56, and (after the small rotation to the field-aligned system) why the fluctuations in Eperon are always smaller than those in Eperoff. We note that the spin axis booms are shorter and thus less affected by finite wavelength effects (which tend to reduce wave power at wavelengths around and below the probe separation distance). If such effects are to be invoked to explain the signal reduction of the longer booms, then a significant portion of the observed wave power must be at wavelengths below ~130 m. The resultant (large) wave vectors are expected to make Doppler shift effects quite prominent. Thus a study of the Doppler shift effect on signal strength deserves immediate attention.

3.1. Amplitude Correction Due to Spacecraft Motion

Plate 6 shows the origin of the aforementioned discrepancy by presenting band-pass-filtered data (48-320 Hz) from probes 1 and 2 (V1 and -V2, referenced to the spacecraft body, denoted by red and blue traces, respectively). In the top panel the signals were collected when sphere 1 is ahead of sphere 2 in the spacecraft direction of motion through the plasma. Conversely, the bottom panel represents a waveform taken half a spin, i.e., 3 s, later, when sphere 1 is behind sphere 2. The electric field Eperon is computed from the sum of these two quantities divided by the interprobe separation (~130 m). It is evident from Plate 6 that the leading signal is from the sphere which lies ahead of the spacecraft in its motion through the plasma. The resultant offset between the peaks and valleys reduces the effective electric field measurement along the 12 direction. A similar temporal offset between the two sphere potentials is also evident in sphere 34 but not in sphere 56 (not shown).

The offset can be thought of as a time lag due to spacecraft motion through spatial (or low-frequency) structures. This is even more evident when the time lag is considered as a function of time. Toward that goal, we constructed the dynamic cross correlation between the V1 and -V2 signals, the V3 and -V4 signals, and the V5 and -V6 signals. This is shown in Plate 7 along with the power spectrum of the corresponding electric field for reference. To construct Plate 7, we high-pass-filtered the signals above 12 Hz and then computed the dynamic power spectra. Additionally, we computed the dynamic cross correlation of 256-point-long stretches (windows) of data. The cross correlation as a function of time lag is the vertical axis of the dynamic cross-correlation plots. The abscissa is the correlation time lag, and the ordinate is the center time of the current window. The peak cross correlation is marked with a dot and is most often very near unity.

It is evident that the peak cross-correlation time lag varies with the window center time as the spheres move from a parallel to an antiparallel position along the spacecraft motion. The peak time lag can be fit with a sine wave of amplitude equal to ~8 ms, which when divided by half the interprobe distance (55 or 65 m) provides the inverse spacecraft velocity (which was ~7.54 km s^{-1} at the time). Note that half the distance must be used, because the probe voltage is referenced to the spacecraft velocity, which makes it effectively an electric field measurement centered at the half of the boom length.

The above observations indicate that the dominant wave power is due to spatial irregularities moving past the spacecraft. They also suggest that a time shift of the raw potential measurements must be made for a correct determination of the electric field amplitude and its spectrum in the spacecraft frame.

This operation is shown in Plate 8. There, the raw potential from the top of Plate 6 is shown again for reference, and the uncorrected electric field is shown just below that (second panel from top). By applying a time lag to the data, i.e., by shifting the time of the measurements to the time they would have been made if the probes were located at the spacecraft body, we remove the effect of the artificial time lag due to spacecraft motion from the data. The corrected electric field computed from the time-lagged potentials is shown in the bottom panel and is significantly larger than before. The time lag between probe voltages computed using the dynamic cross-correlation method is (on average) now zero; this is shown in Plate 9. When the resultant electric field is despun and is cast in the (Epar, Eperon, Eperoff) coordinate system (shown in Plate 10, to be compared to that of Plate 5), then the power of the Eperon component (closest to the ram direction but exactly normal to the field) increases to match the power of the peroff component (normal to ram direction, still normal to the field). The increase in power is evident up to $2 * Vsc/d$, where d is the interprobe separation and is marked with the arrows inserted in Plate 10.

The correction to the E field from the time lag effects applies for all wavelengths. However, for wavelengths longer than $d/2$, and under the assumption of frozen structures moving past the probes, our time lag correction is equivalent to a finite wavelength effect correction. This is because each probe voltage is in effect an electric field measurement between the probe and the spacecraft, of baseline equal to half the interprobe separation. By time shifting the probe voltages to the time they would have been detected at the spacecraft body, we are effectively splitting the double-probe E field measurement to two double-probe measurements of half the baseline. Thus we are effectively removing finite wavelength effects up to $d/2$. At shorter wavelengths, finite wavelength effects overtake, though the time lag correction is still applicable and important. The fact that the break in the spectrum is at $Vsc/(d/2)$ means that our interpretation of the waves as frozen structures being convected past the satellite frame is indeed correct.

The above time lag correction removes neither Doppler shift effects on the measured frequency nor finite wavelength effects beyond wavelengths $d/2$. The first effect, the Doppler shift, is responsible for the appearance of a low-frequency, broad k-spectrum as a broadband frequency spectrum. The second effect can be minimized by spin phase selection; this is taken up in section 3.2.

3.2. Finite Wavelength Effect Corrections

Finite wavelength effects result in a reduced electric field measurement because the probes measure potential differences between crests and troughs of a passing wave of wavelength comparable to (or less than) the probe separation, instead of the instantaneous lo-

cal derivative of the potential structure. In the case of electrostatic waves perpendicularly Polarized to the magnetic field, we can remove the effect of a finite interprobe separation by selecting the spin phase for which one boom pair is near perpendicular to the spacecraft motion. This direction is near the field-aligned direction for cusp perigee crossings. We then assume that the potential drop along the spheres is entirely across the magnetic field, which is equivalent to implementing the $E*B = 0$ approximation, already validated by our measurements. We thus utilize only the near-field-aligned pair and the spin axis pair to obtain a two-dimensional electric field measurement, and we determine the third component of the electric field from the $E * B = 0$ approximation. A sketch of the relative orientations of the booms, spacecraft velocity, and magnetic field are shown in the insert of Plate 11.

When the boom pair is nearly aligned with the magnetic field, then field-aligned electrons may be prohibited from reaching the probe that is behind the spacecraft body, thereby affecting the quality of the potential measurement. Culling of the data from near-field-aligned (<5°) pair orientations needs to accompany our selection of fields near normal to the velocity vector. In addition, Eperp computation from nearly field-aligned probe orientations suffers from increased uncertainty because noise in the field-aligned measurement is amplified by the inverse of the sine of the angle between the boom and the magnetic field. Culling data obtained from within ~10°-15° of the magnetic field direction is necessary to remove such effects. On the basis of the magnetic field average value during the event (see insert in Plate 2) the field is at an angle of 9.8° from the spin plane. Applying an avoidance cone angle of $\Psi > 15°$ around the magnetic field removes the data spikes associated with both electron "shadowing" and increased noise, and results in good-quality measurements.

Plate 11 shows the spectrum of the electric field in the field-aligned coordinate system (Epar, Eperon, Eperoff) with finite wavelength effects reduced by using $\Theta > 60°$ (Θ being the angle between the ram direction and any boom). The maximum effective (along the direction of motion) spin plane intersphere separation is now reduced to $\sin(\Theta)$, i.e., to half the original size (the original size was $d/2$, where $d = 110$ or 130 m depending on boom, because of time lag corrections). The average boom distance during the course of the measurements is even smaller (approximately another factor of 2 smaller), because the boom rotates between Θ and the direction perpendicular to the ram. Thus the average effective length of the booms used for the Eperon computation is ~1/8 of the original 110 and 130 m and very close to the 56 boom size (13 m).

It is evident that the spin plane and spin-normal component spectra match each other, as expected from the same size booms for spacecraft motion through homogeneous, isotropic 2-D turbulence [see *Temerin,* 1979, Figure 3]. The response of the boom 56 (perpendicular to the spacecraft motion) to the low-frequency turbulence comes from Doppler-shifted k-vectors at oblique angles to the spacecraft motion and to the boom direction. The effect is a spectral density at all frequencies that lies within a factor of 2 of the ram direction spectrum. Thus the matching in the corrected spectra in the two directions perpendicular to the magnetic field suggests that the waves seen in the spacecraft frame are indeed homogeneous in these two dimensions.

4. Interpretation

There are several reasons that suggest that the observed waves are due to homogenous, low-frequency, broad k-spectrum spatial structures Doppler-shifted to the observed frequency range owing to the spacecraft motion. These are the following: (1) the obvious dependence of the sphere potential time lags on spacecraft spin phase and the relatively low spread of their cross correlation, (2) the match between finite wavelength effect corrections and the expectation of a critical wavelength equal to Vsc/d or $2 * Vsc/d$ beyond which such effects become important, and (3) the agreement in the cross-field spectra in the spin plane and spin-normal directions. This agreement suggests homogeneity of the observed (low frequency) fluctuations also in the rest frame of the plasma. We adopt this interpretation in this paper.

5. Dominant Mode Frequency

We next examined the spread of the time lags in the cross correlation of the probe potentials about their best (sine) fit. The spread decreases with frequency for a given burst event and varies from one burst event to the other depending on the spectral distribution (predominant frequency) of the event (the higher the spectral density of the high frequencies, the smaller the time lag spread for the specific burst event studied). Plate 12 demonstrates the reduction in time lag spread with frequency for the event of March 18, 1996. This is done by using similar time lags as shown in Plate 9, except for the application of a band-pass filter to the data prior to entire operation of time shifting. Red corresponds to the spin plane spheres (1,2,3,4), and blue corresponds to the spin axis spheres (5,6).

The dependence of time lag spread on frequency may be due to two reasons. In a pure, spatial interpretation of the spectrum, the cross correlation spread is due to uncertainties in the timing of the signal propagating from the one sphere to the other. Higher frequencies, corresponding to shorter wavelengths, result in more refined, more accurate timing in the cross correlation of the sphere potentials for finer-grained spatial irregularities. In this interpretation the spread in the cross correlation around the peak is due to the natural indeterminacy in the arrival of signals at the two antennas, with smoother signals leading to less determined arrival

times and broader cross-correlation peaks.

If a small, temporal variation of the potential exists, i.e., if the signal changes in time between its appearance at the two probes, then finite phase velocity effects add to the correlation spread; the correlation peak time lag will shift away from the one expected from pure spacecraft motion in a manner proportional to the dominant phase velocity in the frame of the plasma at the time the cross correlation was determined. When band-pass-filtered data are used in a particular frequency (wavelength), the typical spread in time lags will be proportional to the typical phase velocities for the wavelength chosen.

For boom orientations near the ram direction the antenna is most sensitive to wavelengths between $b*cos\Theta$ and the maximum wavelength allowable on the basis of the filtering (Θ being the boom-to-ram-direction angle, and b being the boom length). The spread in arrival times at the two probes will be given by $2\delta\tau = b*cos\Theta/(V_{sc}-V_{\rm phase}) - b*cos\Theta/(V_{sc}+V_{\rm phase}) \sim 2(b*cos\Theta/V_{sc})(V_{\rm phase}/V_{sc})$. Note that $2\delta\tau$ is the full width half maximum of the cross correlation time lag distribution, and we assume to first approximation $V_{\rm phase} << V_{sc}$. The two terms come from waves with phase velocities parallel and antiparallel to the spacecraft velocity. As Θ goes close to 90°, the effective distance $b*cos\Theta$ goes to zero, and for finite (measured) $\delta\tau$ the phase velocity should also go to zero. The maximum phase velocity obtained by this technique is given by the $V_{\rm phase}$ in the ram direction. The phase velocity is also a maximum in the sense that if the observed time lag spread is due to indeterminacy due to finite wavelength effects, the resultant temporal effects would be smaller, and our $V_{\rm phase}$ estimate would have to be reduced.

The maximum phase velocity is $V_{\rm phase} = V_{sc}*\delta\tau/\tau_o$, where $\tau_o = b/V_{sc}$ (~8 ms) represents the lag corresponding to the peak cross correlation. For each of the three frequency regimes $f_{\rm band}$ shown in Plate 12, the corresponding wavelengths are $V_{sc}/f_{\rm band}$ ~52, 243, and 1200 m, respectively (we chose the lowest frequency in each frequency band because the spectral power dominates there; in the lowest frequency band the dominant frequency is based on the correlation window size, 0.16 s). Conic thermal velocities (~150 and ~30 km s^{-1} for O^+ and H^+, respectively) and gyrofrequencies given the measured value of the magnetic field (B~9000 nT; f_{O+}~9 Hz, f_{H+}~140 Hz) result in gyroradii of ρ_{O+}~2600 m and ρ_{H+}~34 m for the two species. Thus the proton gyroradius is comparable to the largest wavelength chosen, and the oxygen gyroradius is smaller than the smallest wavelength chosen.

The spreads in time lags corresponding to the three frequency regimes chosen are 1, 2, and 3 ms. The maximum phase velocities we obtain in each wavelength domain for the observed time lags are 0.95, 1.9, and 2.8 km s^{-1}. Using the characteristic wavelength of each frequency band, we obtain the maximum frequency of the oscillation: $f_{\rm max} = V_{\rm phase}/\lambda = 18, 8$, and 2 Hz. Such small frequencies are consistent with our interpretation of the observed spectrum as a wave number spectrum, rather than a frequency spectrum. The observed electric fields are, for the most part, due to Doppler shift of low-frequency (<20Hz) waves. In particular, when the low-frequency (<31Hz), large wavelength (~1200 m) portion of the spectrum is interpreted as partly due to temporal effects, the typical oscillation frequency obtained from the time lag spread is < 2 Hz. This frequency is far below the oxygen gyrofrequency (f_{O+}~ 9 Hz) which prohibits the application of the waves for gyroresonant heating of oxygen. If at least part of the observed time lag spread is due to indeterminacy in signal arrival times arising from long wavelengths relative to boom size, then the dominant wave frequency estimates would have to be revised downward. The maximum oscillation frequencies are also much lower than the typical hydrogen gyrofrequency (f_{H+}~140 Hz).

6. Discussion

Regarding the origin of the observed waves, it is noted that the low frequency and broad k-spectrum of the waves are inconsistent with the ion acoustic and the ion cyclotron instabilities because those have limited perpendicular wave number range when excited by ion beams, loss cone, or electron beams [*Gary,* 1993]. Conversely, the frequent occurrence of density changes during cusp crossings suggests that density gradients may represent a natural free energy source in this region. The broad k-spectrum, small wave number range, and low frequencies of the universal drift instability renders it a natural candidate for the observed spectra. Other instabilities such as the gradient drift instability [*Cerisier et al.,* 1985], shear-driven turbulence [*Basu et al.,* 1988, 1994] are also viable candidates for local wave excitation. Nonlocal wave generation is also a viable candidate if the waves are interpreted as dispersive Alfvén waves [*Louarn et al.,* 1994; *Stasiewicz et al.,* 2000]. The electric field signal quality arrived at after the corrections performed in this paper should permit mode identification especially when taking into account the simultaneously collected magnetic field signal from the PWI and after ensuring appropriately calibrated amplitude and phase responses. In particular, it should be possible to obtain phase relationships between the electric and magnetic field data and differentiate between drift waves and dispersive Alfvén waves. The amplitude ratio of the electric and magnetic field data can then be used to differentiate between inertial and kinetic waves [*Lysak and Lotko,* 1996] based on the different wave number dispersion characteristics of these waves (see, e.g., *Lysak* [1998] for the methodology).

The spectral shape of the corrected spectrum exhibits a break at ~150 Hz. Below that the power falls as f^{-1}, whereas above it falls like $f^{-2.5}$. The anticipated gyroradii of ρ_{O+}~2600 m and ρ_{H+}~34 m of the two species correspond to Doppler-shifted frequencies of 3 and 220

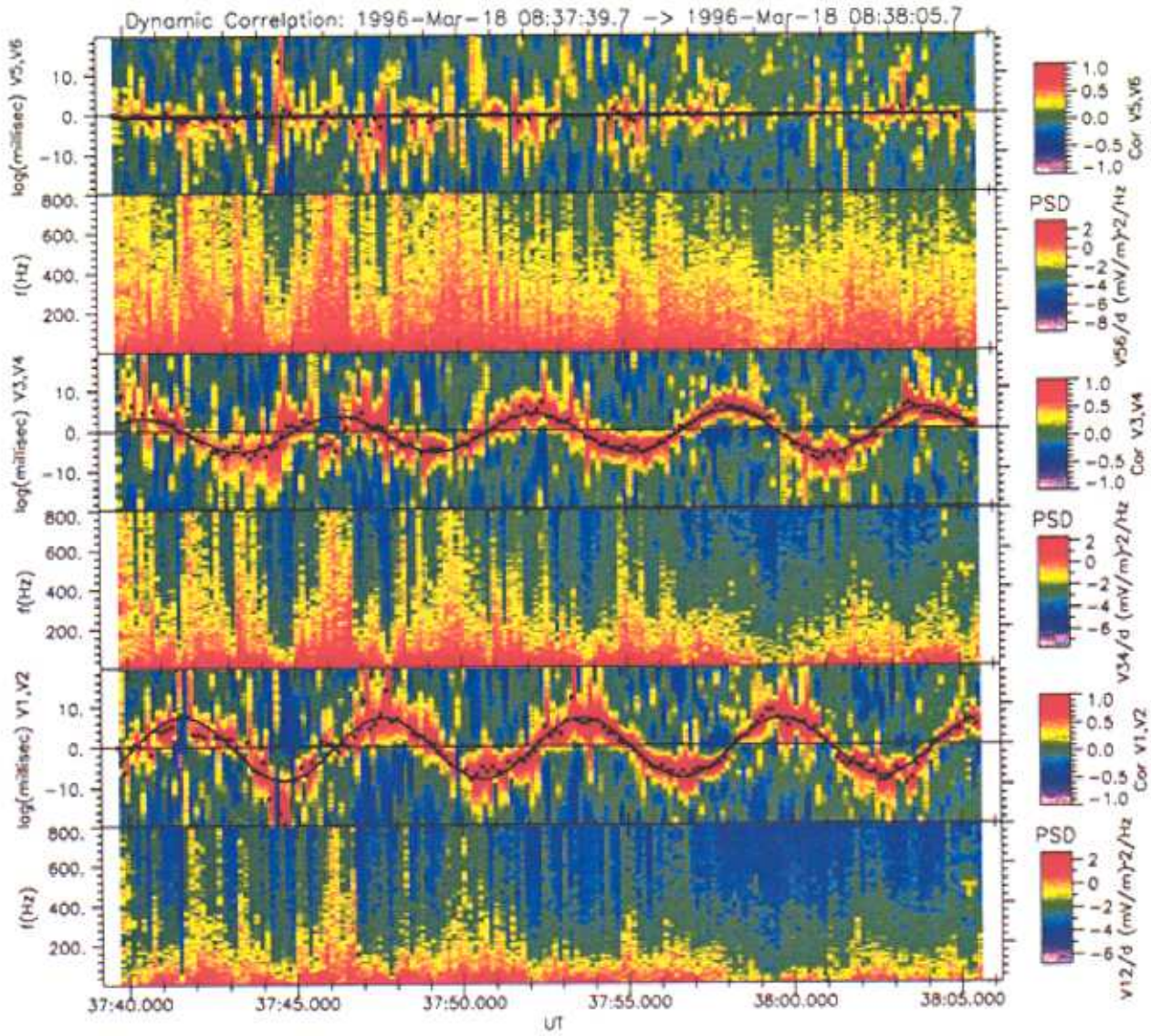

Plate 7. Dynamic cross correlation of each sphere pair potentials and dynamic spectrograms of the electric field computed from them. A window of 256 points (0.16 s) was used for both. The dynamic cross correlation shows that the peak time lag (ms) is a sinusoidal function of spin phase for sphere pairs 12 and 34, owing to the sphere motion in and out of the ram direction, but the peak time lag does not depend on time for the 56 pair. This is evidence of spacecraft motion through spatial irregularities producing a time lag with amplitude proportional to the boom length and inversely proportional to the spacecraft velocity. The peak time lag amplitude is larger for sphere pair 12 than for 34, since booms 1 and 2 are longer (65 m) than booms 3 and 4 (55 m). The power of the E56 signal is larger than that of E34, which in turn is larger than that of E12, owing to two effects: the reduction of the electric field due to the aforementioned time lag effect and the finite wavelength effect.

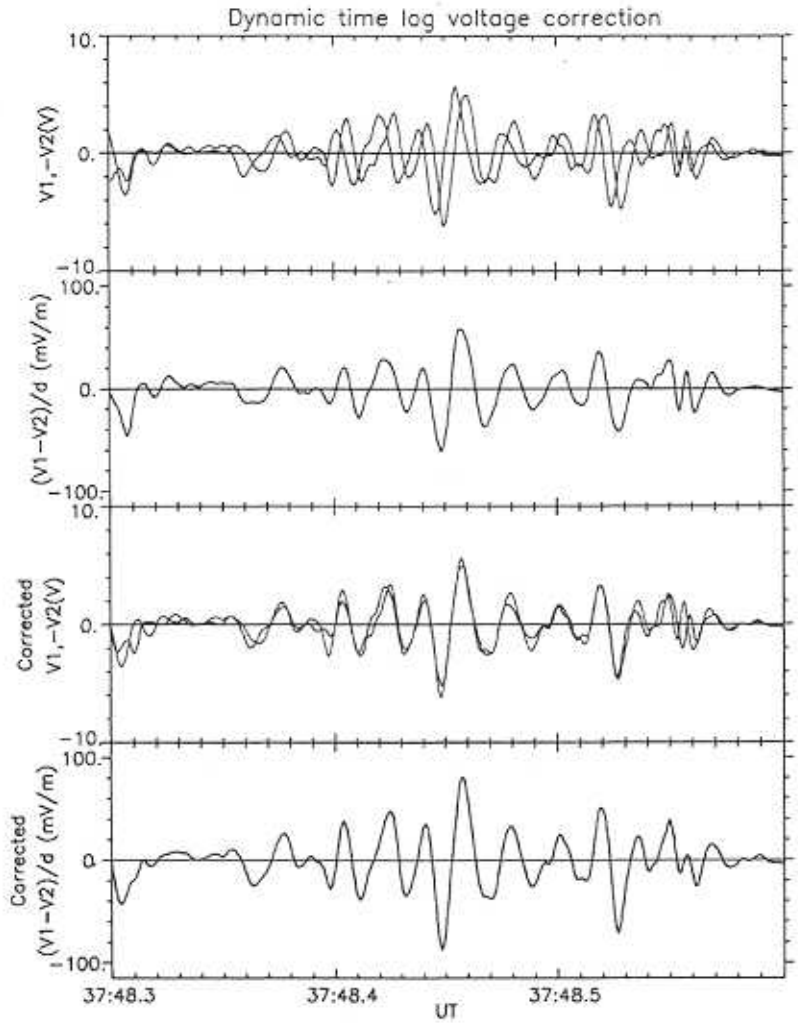

Plate 8. Correction of electric field signal for time lag effect. The first panel shows the sphere potentials of Plate 5 (top) for reference, and the second panel shows the electric field computed from them. When each potential measurement's time is corrected to correspond to the time when the structure would have passed by the satellite body, the two potential measurements agree quite well (third panel from top). The electric field computed from the sum of the two quantities (V1 and -V2) is now larger than before (fourth panel).

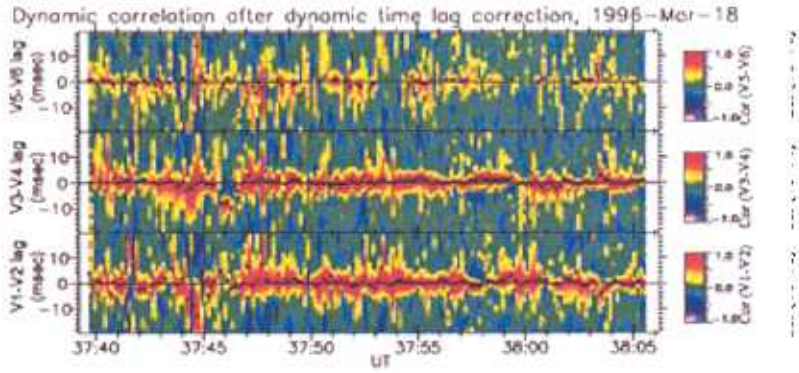

Plate 9. Confirmation of the dynamic time lag correction, showing how repeating the dynamic cross correlation to the corrected signal leads to a zero average time lag. To be compared to Plate 6.

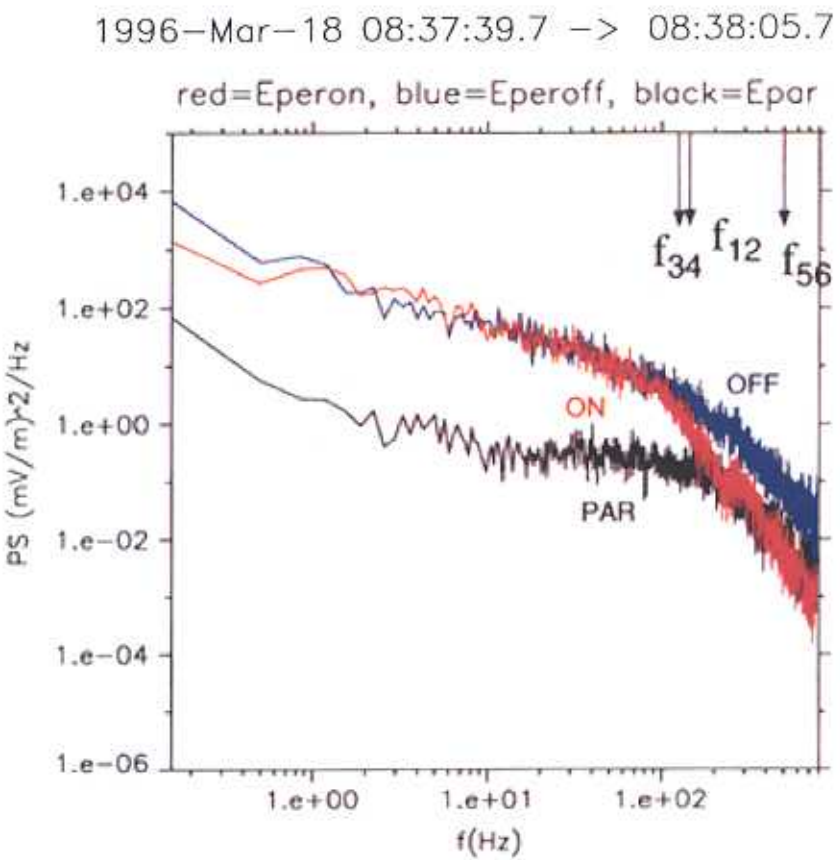

Plate 10. Power spectral density for the quantities Epar, Eperon and Eperoff, computed from the electric field signals corrected for the time lag effect. The correction applied also removes finite wavelength effects up to wavelengths of $d/2$, because a sphere probe measures the plasma potential referenced to the spacecraft body and is (effectively) an electric field measurement of baseline $d/2$. Finite wavelength effects cannot be removed to below that wavelength through the time lag correction alone. Plate 10 is to be compared to Plate 4. Frequency inserts f_{12} and f_{34} are the Doppler-shifted frequencies where finite wavelength effects start appearing for pairs 12 and 34.

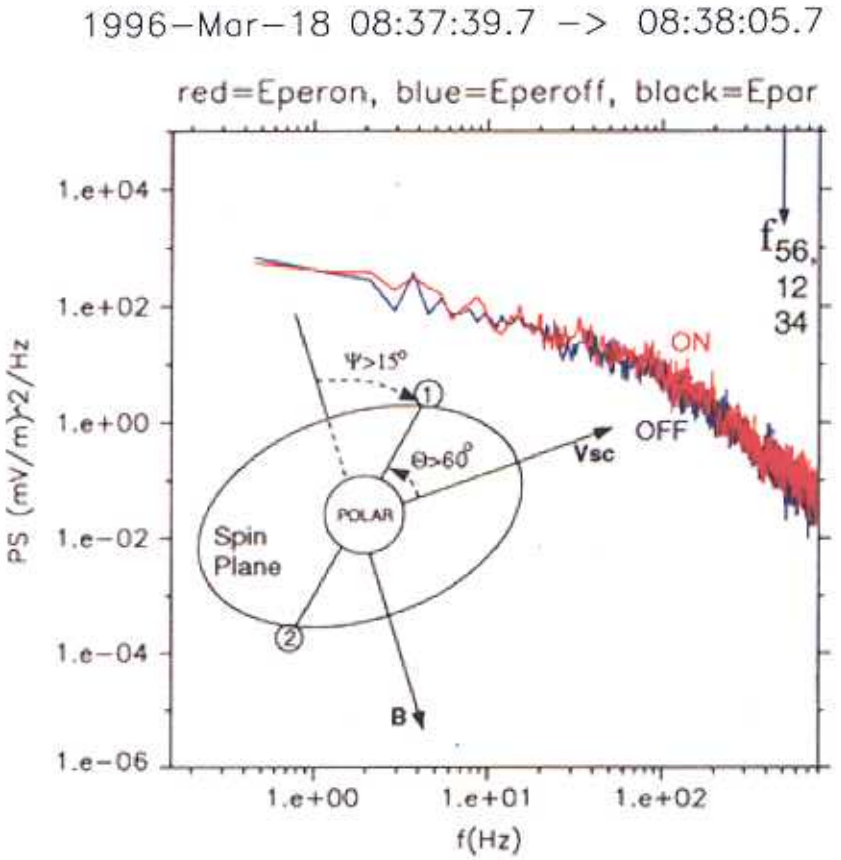

Plate 11. Power spectral density of Eperon, and Eperoff, after finite wavelength effect correction by spin phase selection. Only the boom pair that was away from the spacecraft velocity vector (by more than 60°) but not too close to the ambient magnetic field vector (not closer than 15°) was used. The assumption of $\mathbf{E} \cdot \mathbf{B}=0$ was employed to compute the electric field perpendicular to the magnetic field. Epar is zero by definition, while the Eperon and Eperoff power spectral densities agree to within a factor of 2, as expected from the response of equal size antennas moving along and across two-dimensional turbulence. Plate 11 is to be compared to Plate 9. Frequencies f_{12}, f_{34}, and f_{56} correspond to the Doppler-shifted frequencies where finite wavelength effects start becoming important.

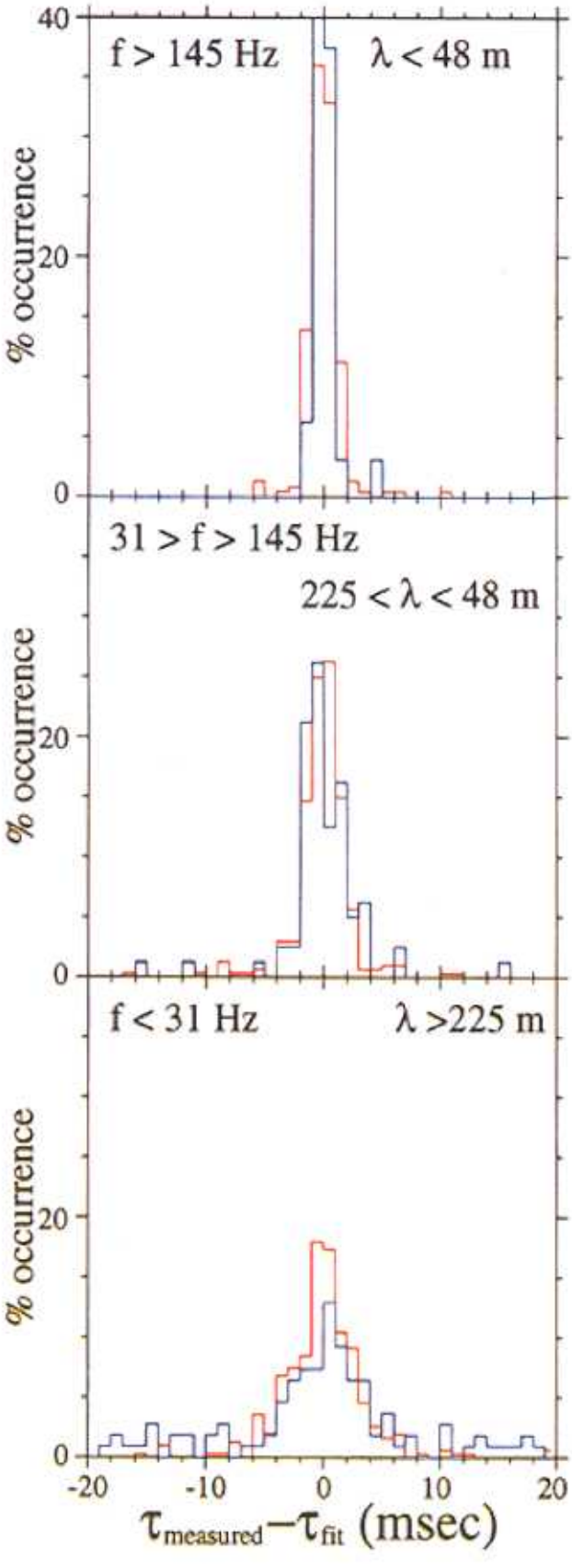

Plate 12. Histograms of measured time lag minus the sine fit to the time lag. This shows essentially the spread in the time lag around the value anticipated from spacecraft motion through spatial irregularities. Different panels correspond to the application of different filters to the raw data.

Hz for O^+ and H^+, respectively. Thus the break in the spectrum corresponds to the Doppler-shifted proton gyroradius. It is possible that this break represents the dissipation length of the excited turbulence.

7. Conclusions

We have used burst-mode electric field data collected on the Polar satellite from the EFI to identify the most commonly observed wave type in crossings of the Polar cusp, namely broadbanded low-frequency waves. We pointed out that even a small fraction of the observed wave power, when interpreted in the temporal domain, could heat the ions via gyroresonant heating, resulting in the concurrently observed ion conics. However, although the apparent wave power is large at the ion gyrofrequencies, ion beams are typically also seen in conjunction with the waves, and the ion conics are typically at an angle far from perpendicular to the magnetic field. This suggests that the heating process occurs below the observation altitude and that the apparently broadbanded waves colocated on the same field lines may not be responsible for the observed heating at that altitude.

We resolved the presence of excessive power in the temporal domain in the following way: We showed that the individual sphere potentials exhibit a time lag suggesting spacecraft motion through spatial structures. When the time lag is properly corrected, the resultant wave powers from the along-track and cross-track booms agree with each other up to frequencies corresponding to Doppler-shifted wavelengths where finite wavelength effects start becoming important. When those finite wavelength effects are amended as well (by selection in spin phase angle), the differences in power between along-track and cross-track spectra are small and comparable to those expected from spacecraft motion through stationary turbulence.

Finally, we examined the spread in cross correlation as evidence of temporal effects in the observed wave power. By interpreting the spread in time lags as perturbations to the intersphere travel time arising entirely from finite phase velocities, we were able to obtain an upper limit to the phase velocities at various frequency bands (corresponding to various wavelengths). These small phase velocities, when divided by the anticipated wavelengths, provide estimates of the maximum dominant wave frequency, in the case of the presence of a temporal component to the time series of sphere potentials. Our frequency estimates are $f_{\max} = V_{\text{phase}}/\lambda = 18, 8$, and 2 Hz for wavelengths of 52, 243, and 1200 m, respectively. Owing to the smallness of our frequency estimates, we conclude that the observed perturbations in the spacecraft frame correspond to Doppler-shifted, low-frequency, two-dimensional isotropic turbulence, rather than being due to temporal fluctuations in the plasma frame. Typical magnetic field values (B~9000 nT) produce f_{H^+}~140 Hz and f_{O^+}~9 Hz and suggest that the gyroresonant heating mechanism cannot be invoked using these waves.

Acknowledgment. Useful discussions with M. André are gratefully appreciated. This work was supported by NASA contract NAS5-30367. We wish to thank C. T. Russell, D. A. Gurnett, and their teams for providing ancillary magnetometer data from the MFE and PWI instruments.

Hiroshi Matsumoto thanks C. T. Russell and another referee for their assistance in evaluating this paper.

References

André, M., and A. Yau, Theories and observations of ion energization and outflow in the high latitude magnetosphere, *Space Sci. Rev., 80,* 27, 1997.

André, M., M. Temerin, and D. Gorney, Resonant generation of ion waves on auroral field lines by positive slopes in ion velocity space, *J. Geophys. Res., 91,* 3145, 1986.

André, M., H. Koskinen, G. Gustafsson, and R. Lundin, Ion waves and upgoing ion beams observed by the Viking satellite, *Geophys. Res. Lett., 14,* 463, 1987.

André, M., H. Koskinen, L. Matson, and R. Erlandson, Local transverse ion energization in and near the Polar cusp, *Geophys. Res. Lett, 15,* 107, 1988.

André, M., G. B. Crew, W. K. Peterson, A. M. Persoon, C. J. Pollock, and M. J. Engebretson, Ion heating by broadband low-frequency waves in the cusp/cleft, *J. Geophys. Res., 95,* 20,809, 1990.

André, M., P. Norqvist, A. Vaivads, L. Eliasson, O. Norberg, A. I. Eriksson, and B. Holback, Transverse ion energization and wave emissions observed by the Freja satellite, *Geophys. Res. Lett., 21,* 1915, 1994.

André, M., P. Norqvist, L. Anderson, L. Eliasson, A. I. Eriksson, L. Blomberg, R. E. Erlandson, and J. Waldemark, Ion energization mechanisms at 1700 km in the auroral region, *J. Geophys. Res., 103,* 4199, 1998.

Basu, S., S. Basu, E. MacKenzie, P. F. Fougere, W. R. Coley, N. C. Maynard, J. D. Winningham, M. Sigiura, W. B. Hanson, and W. R. Hoegy, Simultaneous density and electric field fluctuation spectra associated with velocity shears in the auroral oval, *J. Geophys. Res., 93,* 115, 1988.

Basu, S., S. Basu, P. K. Chaturvedi, and C. M. Bryant Jr., Irregularity structures in the cusp/cleft and Polar cap regions, *Radio Sci., 29,* 195, 1994.

Cerisier, J. C., J. J. Berthelier, and C. Beghin, Unstable density gradients in the high-latitude ionosphere, *Radio Sci., 20,* 755, 1985.

Chang, T., G. B. Crew, N. Hershkowitz, J. R. Jasperse, J. M. Retterer, and J. D. Winningham, Transverse acceleration of oxygen ions by electromagnetic ion cyclotron resonance with broad band left-hand Polarized waves, *Geophys. Res. Lett., 13,* 636, 1986.

Ergun, R. E., et al., FAST satellite observations of electric field structures in the auroral zone, *Geophys. Res. Lett., 25,* 2025, 1998a.

Ergun, R. E., et al., FAST satellite observations of solitary structures, *Geophys. Res. Lett., 25,* 2041, 1998b.

Gary, S. P., Theory of Space Plasma Microinstabilities, Cambridge Univ. Press, New York, 1993.

Gurnett, D. A., and T. B. Burns, The low frequency cutoff of ELF emissions, *J. Geophys. Res., 73,* 7437, 1968.

Gurnett, D. A., and L. A. Frank, VLF hiss and related plasma observations in the Polar magnetosphere, *J. Geophys. Res., 77,* 172, 1972.

Gurnett, D. A., R. Huff, R. L. Mennietti, J. D. Burch, J. L. Winningham, and S. D. Shawhan, Correlated low-

frequency electric and magnetic noise along the auroral field lines, *J. Geophys. Res., 89,* 8971, 1984.

Gurnett, D. A., et al., The Polar plasma wave instrument, *Space Sci. Rev., 71,* 597, 1995.

Harvey, P., et al., The electric field instrument on the Polar satellite, *Space Sci. Rev., 71,* 583, 1995.

Huddleston, M. M., C. J. Pollock, M. P. West, J. S. Pickett, T. E. Moore, and W. K. Peterson, Torroidal ion distributions observed at high altitudes equatorward of the cusp, *Geophys. Res. Lett., 27,* 469, 2000.

Kintner, P. M., J. Bonnell, R. Arnoldy, K. Lynch, C. Pollock, and T. Moore, SCIFER-Transverse ion acceleration and plasma waves, *Geophys. Res. Lett., 23,* 1873, 1996.

Louarn, P., et al., Observations of kinetic Alfvén waves by the FREJA spacecraft, *Geophys. Res. Lett., 21,* 1847, 1994.

Lysak, R.L., The relationship between electrostatic shocks and kinetic Alfvén waves, *Geophys. Res. Lett., 25,* 2089, 1998.

Lysak, R. L., and W. Lotko, On the kinetic dispersion relation for shear Alfvén waves, *J. Geophys. Res., 101,* 5085, 1996.

Moore, T. E., et al., The thermal ion dynamics experiment and plasma source instrument, *Space Sci. Rev., 71,* 409, 1995.

Mozer, F. S., et al., Observations of paired electrostatic shocks in the Polar magnetosphere, *Phys. Rev. Lett., 38,* 292, 1977.

Mozer, F. S., et al., New features of time domain electric-field structures in the auroral acceleration region, *Phys. Rev. Lett., 79,* 1281, 1997.

Peterson, W. K., E. G. Shelley, S. A. Boardsen, and D. A. Gurnett, Transverse auroral ion energization observed on DE-1 with simultaneous plasma wave and ion composition measurements, in *Ion Acceleration in the Magnetosphere and Ionosphere, Geophys. Monogr. Ser.,* vol. 38, edited by T. Chang, p. 43, AGU, Washington, D.C., 1986.

Russell, C. T., and R. E. Holzer, AC magnetic fields, in *Particles and fields in the magnetosphere,* edited by B. M. McCormac, p. 195, D. Reidel, Dordrecht, Netherland, 1970.

Russell, C. T., R. C. Snare, J. D. Means, D. Pierce, D. Dearborn, M. Larson, G. Barr, and G. Le, The GGS/Polar magnetic fields investigation, *Space Sci. Rev., 71,* 563, 1995.

Shelley, E. G., et al., The toroidal imaging mass-angle spectrograph (TIMAS) for the Polar mission, *Space Sci. Rev., 71,* 497, 1995.

Stasiewicz, K., Y. Khotyaintsev, M. Berthomier, and J.-E. Wahlund, Identification of widespread turbulence of dispersive Alfvén waves, *Geophys. Res. Lett., 27,* 173, 2000.

Temerin, M., The Polarization, frequency, and wavelengths of high-latitude turbulence, *J. Geophys. Res., 83,* 2609, 1978.

Temerin, M., Doppler shift effects on double-probe-measured electric field power spectra, *J. Geophys. Res., 84,* 5929, 1979.

Temerin, M., and R. L. Lysak, Electromagnetic ion cyclotron mode (ELF) waves generated by auroral electron precipitation, *J. Geophys. Res., 89,* 2849, 1984.

Temerin, M., M. Woldorff, and F. S. Mozer, Nonlinear steepening of the electrostatic ion cyclotron wave, *Phys. Rev. Lett., 43,* 1941, 1979.

Yau, A., and M. André, Sources of ion outflow in the high latitude ionosphere, *Space Sci. Rev., 80,* 1, 1997.

V. Angelopoulos, J. Bonnell, F. S. Mozer, M. Somoza, and M. Temerin, Space Sciences Laboratory, University of California, Berkeley, CA 94720-7450. (vassilis@ssl.berkeley.edu)

H. L. Collin and W. K. Peterson, Lockheed Martin Space Physics Laboratory, Palo Alto, CA 94304-1191. (collin@mail.spasci.com; pete@spasci.com)

B. Giles, NASA Goddard Space Flight Center, Greenbelt, MD 20771. (Barbara.L.Giles.1@gsfc.nasa.gov)

(Received May 18, 2000; revised July 25, 2000;
accepted September 7, 2000.)